nanomaterials

MDPI

Article

Modulating Ni/Ce Ratio in $Ni_yCe_{100-y}O_x$ Electrocatalysts for Enhanced Water Oxidation

Jun Yu [1,2,3], Qi Cao [1,3,*], Chen Qiu [2,4], Lei Chen [4,*] and Jean-Jacques Delaunay [3,*]

1 Key Laboratory of Energy Thermal Conversion and Control, and Key Laboratory of Environmental Medicine Engineering of Ministry of Education, School of Energy and Environment, Southeast University, Nanjing 210096, China; yujun12@mails.tsinghua.edu.cn
2 Guangdong Key Lab of Nano-Micro Materials Research, School of Chemical Biology and Biotechnology, Peking University Shenzhen Graduate School, Shenzhen 518055, China; qiuc12@163.com
3 Graduate School of Engineering, The University of Tokyo, 7-3-1 Hongo, Bunkyo-ku, Tokyo 113-8656, Japan
4 State Key Laboratory of Tribology, Tsinghua University, Beijing 100084, China
* Correspondence: qicao@seu.edu.cn (Q.C.); leichen16@mail.tsinghua.edu.cn (L.C.); jean@mech.t.u-tokyo.ac.jp (J.-J.D.)

Abstract: Oxygen evolution reaction (OER) is the key reaction for water splitting, which is used for hydrogen production. Oxygen vacancy engineering is an effective method to tune the OER performance, but the direct relationship between the concentration of oxygen vacancy and OER activity is not well understood. Herein, a series of $Ni_yCe_{100-y}O_x$ with different concentration of oxygen vacancies were successfully synthesized. The larger concentration of oxygen vacancies in $Ni_{75}Ce_{25}O_x$ and $Ni_{50}Ce_{50}O_x$ result in their lower Tafel slopes, small mass-transfer resistance, and larger electrochemical surface areas of the catalysts, which account for the higher OER activities for these two catalysts. Moreover, with a fixed current density of 10 mA/cm^2, the potential remains stable at 1.57 V for more than 100 h, indicating the long-term stability of the $Ni_{75}Ce_{25}O_x$ catalyst.

Keywords: oxygen evolution reaction (OER); $Ni_yCe_{100-y}O_x$; oxygen vacancies

Citation: Yu, J.; Cao, Q.; Qiu, C.; Chen, L.; Delaunay, J.-J. Modulating Ni/Ce Ratio in $Ni_yCe_{100-y}O_x$ Electrocatalysts for Enhanced Water Oxidation. *Nanomaterials* **2021**, *11*, 437. https://doi.org/10.3390/nano11020437

Academic Editor: Diego Cazorla-Amorós
Received: 30 December 2020
Accepted: 5 February 2021
Published: 9 February 2021

1. Introduction

Hydrogen is considered as one of the clean energy to replace the traditional fossil fuel to solve the environmental and energy problem. Electrocatalytic water splitting is an effective way to produce hydrogen with high purity from intermittent renewable energy (i.e., wind and solar energy). Two half reactions including hydrogen evolution reaction (HER) and oxygen evolution reaction (OER) are at cathode and anode, respectively. The four-electron transfer steps of OER lead to the large sluggish kinetics, resulting in a high overpotential for water splitting [1–7]. An OER catalyst with high activity is of critical importance to reduce the overpotential so that a small bias voltage can be used and thus increase the efficiency of the OER process.

The OER activity of a catalyst can be enhanced by introducing defects, especially oxygen vacancies [8–11]. The local electron density distribution will be changed and the oxygen vacancy itself can be the OER active sites. Wang et al. [12] treated Co_3O_4 nanosheets by Ar-plasma to get rich oxygen vacancies. The specific activity of the Co_3O_4 nanosheets with oxygen vacancies was 10 times higher than that of the pristine Co_3O_4. Ceria is a nonstoichiometric material and the oxygen vacancies are easily formed due to the shift between Ce^{3+} and Ce^{4+} [13–17]. The oxygen vacancies in Ce-containing catalysts such as CeO_2/Co_3O_4 accelerated the electron transfer, resulting in good OER activity [9]. In our previous work, oxygen vacancies in $NiCeO_x$ catalyst were proved to be the active sites for water oxidation [10]. However, the direct correlation between the concentration of oxygen vacancies and OER activity has not been identified yet.

In this work, a series of $Ni_yCe_{100-y}O_x$ with different Ni/Ce ratio were synthesized on NF (nickel foam)/NiO substrate with simple dip-coating and annealing methods. The

surface NiO obtained from the oxidation of NF can prohibit the diffusion of Ni atoms to the deposited $Ni_yCe_{100-y}O_x$ so that the Ni/Ce ratio is not modified. Oxygen vacancy defects are formed successfully in all the NF/NiO/$Ni_yCe_{100-y}O_x$ (simply referred to as $Ni_yCe_{100-y}O_x$) catalysts. The concentration of oxygen vacancy defects for $Ni_{75}Ce_{25}O_x$ and $Ni_{50}Ce_{50}O_x$ catalysts are larger than other $Ni_yCe_{100-y}O_x$ catalysts, resulting in a similar larger electrochemically active surface area and the same lower Tafel slope of 66 mV/decade. The overpotential to achieve a current density of 10 mA/cm^2 for the $Ni_{75}Ce_{25}O_x$ and $Ni_{50}Ce_{50}O_x$ catalysts are 338 mV and 341 mV, respectively. It is noted that these overpotentials are lower than other $Ni_yCe_{100-y}O_x$ catalysts. With a fixed current density of 10 mA/cm^2, the $Ni_{75}Ce_{25}O_x$ catalyst exhibits an ultra-high stability of over 100 h.

2. Materials and Methods

2.1. Sample Synthesis

The synthesis of NF/NiO/$Ni_yCe_{100-y}O_x$ catalysts. The first step was to prepare the NF/NiO substrate. A 10 × 15 mm^2 Nickel Foam (NF, >99.99%, MTI Corporation, Richmond, CA, USA) substrate with a thickness of 0.08 mm was firstly cleaned by acetone (99%, Wako) in an ultrasonic bath for 5 min. Then the NF was rinsed by deionized water three times. Subsequently, the NF was dried in air and annealed for 2 h with a heating rate of 2 °C/min at 400 °C in a muffle furnace to obtain NF/NiO substrate. The second step is to prepare the nickel and cerium mixed precursor solution. The precursor solution was prepared by dissolving 0.3 M citric acid and 0.15 M metal ions in 20 mL ethanol. The molar ratio of Ni and Ce ions were 95:5, 90:10, 75:25, 50:50, 25:75, and 10:90 for the catalysts of $Ni_{95}Ce_5O_x$, $Ni_{90}Ce_{10}O_x$, $Ni_{75}Ce_{25}O_x$, $Ni_{50}Ce_{50}O_x$, $Ni_{25}Ce_{75}O_x$ and $Ni_{10}Ce_{90}O_x$, respectively. $Ce(NO_3)_3$ $6H_2O$ offers the Ce ions and $Ni(NO_3)_2$ $6H_2O$ offers the Ni ions. The final step is the preparation of NF/NiO/$Ni_yCe_{100-y}O_x$ catalysts, hereafter simply referred to as the $Ni_yCe_{100-y}O_x$. The prepared precursor solution was deposited onto NF/NiO by dip coating and then annealed in the same manner as the NF/NiO substrate.

2.2. Structural Characterization

A field emission Scanning electron microscope (SEM, JEOL JSM 7600 FA) was used for the measurements of SEM. A diffractometer (Rigaku Co. Ltd., SmartLab, Japan) with Cu Kα radiation (dwelling time = 2 s, incident angle = 0.5°, step size = 0.02°, λ = 1.541 Å) was used for the collecting of grazing incidence X-ray diffraction data. A Renishaw inVia Raman Microscope system was used to acquire the Raman spectra at room temperature (25 °C). A ×100 objective and a 532 nm excitation laser were used. A PHI 5000 VersaProbe (ULVAC-PHI) with an Al Kα X-ray source (1486.6 eV) was used to obtain the X-ray photoelectron spectroscopy (XPS). The pass energies of 117.4 eV and 23.5 eV were used for the electron analyzer to analyze the wide scans and narrow scans, respectively.

2.3. Electrochemical Measurements

A cylindrical glass cell with a standard three-electrode configuration was used for the electrochemical measurements. A Pt wire and a Ag/AgCl electrode were used as the counter electrode and the reference electrode, respectively. The working electrode was $Ni_yCe_{100-y}O_x$ electrode. A potentiostat (Princeton Applied Research, VersaSTAT 4) was used to perform the electrochemical measurements. The potentials were calibrated against the RHE according to the following equation: ($E_{RHE} = E_{Ag/AgCl} + 0.059\ pH + E^0{}_{Ag/AgCl}$), where $E_{Ag/AgCl}$ is the potential difference measured between the Ag/AgCl electrode and the working electrode, $E^0{}_{Ag/AgCl}$ (0.1976 V at 25 °C) is the standard electrode potential for an Ag/AgCl electrode, pH is the pH of the electrolyte solution, and E_{RHE} is the calibrated potential. The electrolytes used were saturated with oxygen before and during the OER experiments.

The polarization curves were collected through linear sweep voltammetry (LSV), and the scan rate was 10 mV/s. Controlled-current water electrolysis was performed using a

chronopotentiometric technique [16]. The solution resistance R_s (~2 Ω), determined using the electrochemical impedance spectroscopy (EIS) technique [16], was used to correct the *iR* drop across the solution. Unless otherwise stated, all given potentials are vs. RHE and corrected for the *iR* drop across the electrolyte. Tafel plots obtained from the steady-state polarization curves with a scan rate of 1 mV/s. Cyclic voltammetry (CV) was used to determine the electrochemical capacitance of the samples presented in this paper [18]. The potential was swept in a range from 0.05 V above the open-circuit potential (OCP) to 0.05V below the OCP in a static solution with five different scan rates: 0.005, 0.01, 0.025, 0.05 and 0.1 V s^{-1}. The working electrode was held for 10 s at each end of the potential sweep before continuing to the next sweep. All experiments were performed at room temperature.

3. Results and Discussion

The surface morphology information of the NF/NiO and $Ni_yCe_{100-y}O_x$ samples was analyzed by SEM, and the images are shown in Figure 1. Holes with sizes varying from several nanometers to a few hundred nanometers were observed on the surface of NF/NiO. NF/NiO sample was prepared by annealing Ni substrate in the muffle furnace for 2 h with the elevating rate of 2 °C/min, and these holes were from the Ni foam substrate. The surface of NF/NiO consisted of small nanocrystals, as shown in Figure 1b. The $Ni_yCe_{100-y}O_x$ samples were synthesized by depositing nickel and cerium mixed precursor solutions with different Ni/Ce ratios on NF/NiO and then annealing the samples in air. The deposited layer covers the surface of NF/NiO nanocrystals for the $Ni_{95}Ce_5O_x$ sample, as shown in Figure 1c,d. Other $Ni_yCe_{100-y}O_x$ catalysts have the similar morphologies with the $Ni_{95}Ce_5O_x$ catalyst, as displayed in Figure S1 of the supporting information.

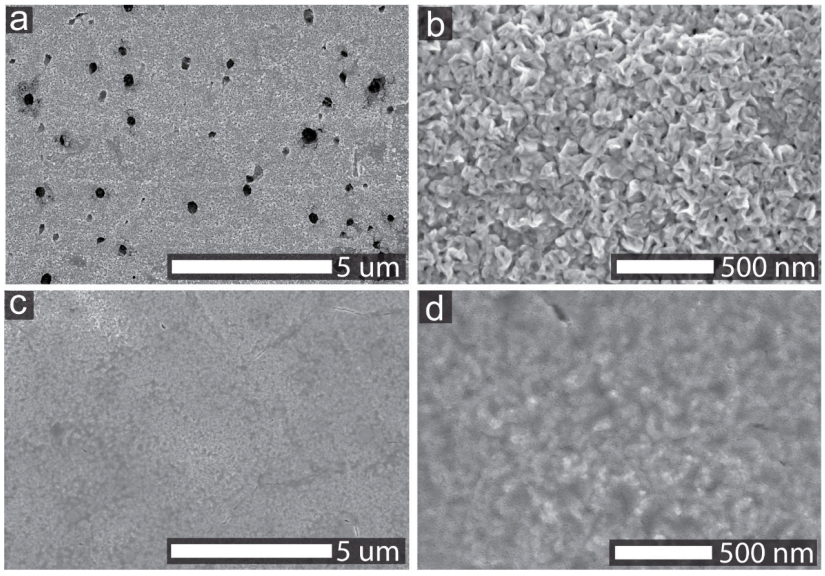

Figure 1. SEM images of NF/NiO (**a**,**b**) and $Ni_{95}Ce_5O_x$ (**c**,**d**) samples.

Grazing incidence XRD measurements were performed to examine the crystal structure of the $Ni_yCe_{100-y}O_x$ samples, and the results are shown in Figure 2a. Only Ni and NiO related peaks were found and no CeO_2 related peaks were detected for $Ni_yCe_{100-y}O_x$ samples. It indicates that Ni and Ce mixed uniformly in the top layer and formed an amorphous structure. The surface element information of the $Ni_yCe_{100-y}O_x$ samples was further analyzed by XPS. As shown in Figure 2b, Ce 3d peaks of CeO_2 and Ni 2p peaks of NiO were observed and indicates that the deposited layers of $Ni_yCe_{100-y}O_x$ catalysts are indeed composed of Ni and Ce mixed oxides. The curve fitting results of Ce $3d_{3/2}$ for $Ni_yCe_{100-y}O_x$ samples are shown in Figure 2c. The peak areas of Ce $3d_{3/2}$ for $Ni_{90}Ce_{10}O_x$, $Ni_{75}Ce_{25}O_x$, $Ni_{50}Ce_{50}O_x$, $Ni_{25}Ce_{75}O_x$ and $Ni_{10}Ce_{90}O_x$ samples are 31.7, 55.7, 206.2, 433.0 and 603.3. For $Ni_yCe_{100-y}O_x$ samples, the peak areas of Ce $3d_{3/2}$ are in proportion with

the Ce content, and the higher Ce content will lead to larger peak areas of Ce $3d_{3/2}$. The sequence of the peak areas of Ce $3d_{3/2}$ of $Ni_yCe_{100-y}O_x$ samples are in accordance with the Ce content in these samples (Table S1). This indicates that the designed Ni/Ce ratios remain constant for the synthesized $Ni_yCe_{100-y}O_x$ samples.

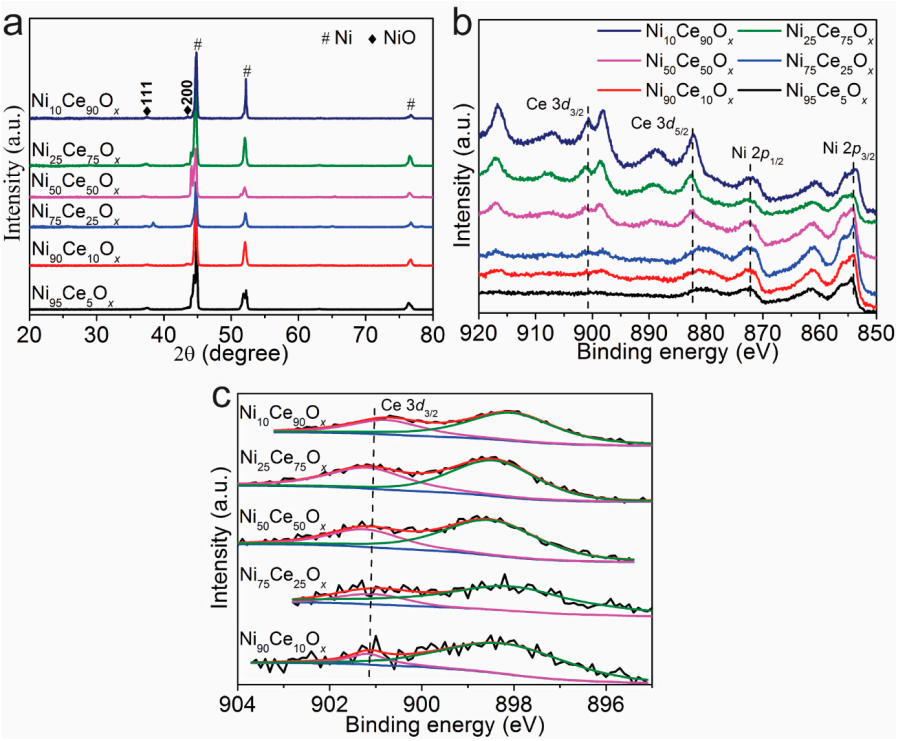

Figure 2. (**a**) X-ray diffraction patterns and (**b**,**c**) XPS spectra of $Ni_yCe_{100-y}O_x$ samples.

Two Raman peaks of 224 cm^{-1} and 563 cm^{-1} were observed for $Ni_{75}Ce_{25}O_x$, $Ni_{50}Ce_{50}O_x$, $Ni_{25}Ce_{75}O_x$ and $Ni_{10}Ce_{90}O_x$ samples, as shown in Figure 3a. For $Ni_{95}Ce_5O_x$ and $Ni_{90}Ce_{10}O_x$ samples, only the peak of 563 cm^{-1} was observed. Crystalline CeO_2 is known to have a strong F_{2g} Raman peak at 464 cm^{-1} related to its fluorite structure [19]. The presence of ions with the oxidation states lower than Ce^{4+} in the CeO_2 has been shown to induce a Raman band, known as the D band, from 500 to 700 cm^{-1} [19–21]. This band is associated with the presence of oxygen vacancy defects created in the non-stoichiometric CeO_{2-y} by the 3+ coordinated ions. In addition to the introduction of the D band, the F_{2g} band will be weakened and becomes asymmetric and broad [22]. In the Raman spectra of the $Ni_yCe_{100-y}O_x$ samples, there is no F_{2g} band, which suggests that there is no crystalline CeO_2 with a fluorite structure in these samples [23]. The broad peak at 563 cm^{-1} (D band) indicates the formation of oxygen vacancy defects. The oxygen vacancy defects should be related to the presence of Ce^{3+} because of the incorporation of Ni into CeO_2, as suggested by the literature [19,20,23]. Furthermore, the amorphous structure of $Ni_yCe_{100-y}O_x$ contributes to the broadness of the peak [22,23]. According to the areas of this peak among different $Ni_yCe_{100-y}O_x$ samples, we can roughly estimate the concentration of oxygen vacancy defects in these catalysts. The peak areas of the D band have been calculated and summarized in Table S2. The peak areas of 563 cm^{-1} for $Ni_{75}Ce_{25}O_x$ and $Ni_{50}Ce_{50}O_x$ samples are similar and larger than those of other $Ni_yCe_{100-y}O_x$ samples, suggesting that these two catalysts own larger concentration of oxygen vacancy defects. The peak at 224 cm^{-1} is related to Ce-OH vibrations which are resulted from surface defects. Different types of hydroxyl groups generated by the dissociation of surface adsorbed water and doubly bridging hydroxyl groups on reduced cerium oxide are detected in the Raman spectra [24].

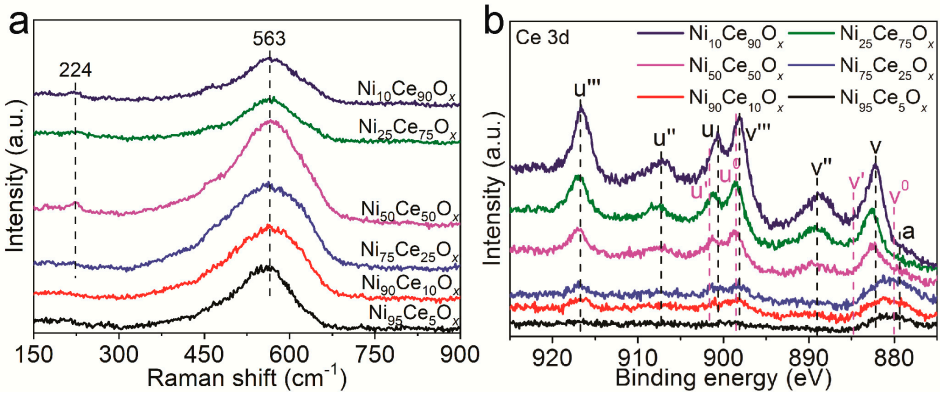

Figure 3. (**a**) Raman spectra and (**b**) XPS spectra of $Ni_yCe_{100-y}O_x$ samples. The peak labeled *a* in the XPS spectra is ascribed to the Ni 2p peak.

XPS was carried out on $Ni_yCe_{100-y}O_x$ samples to further analyze the oxygen vacancy defects. The Ce 3d peaks of CeO_2 were observed for $Ni_yCe_{100-y}O_x$ samples, as shown in Figure 3b. The Ce 3d band is composed of ten individual peaks, that are labeled on Figure 3b as v, v'', v''', u, u'', u''', v^0, v', u^0 and u'. The v, v'', v''', u, u'' and u''' peaks represent the $3d^{10}4f^0$ state of Ce^{4+}, and the v^0, v', u^0 and u' peaks represent the $3d^{10}4f^1$ state of Ce^{3+} [13,25]. The intensities of these peaks increased with the increasing Ce content in $Ni_yCe_{100-y}O_x$ samples. The concentration of Ce^{3+} and Ce^{4+} can be estimated according to the relative areas of the corresponding peaks. The major valence state of Ce was 4+, Ce^{3+} were also detected for $Ni_yCe_{100-y}O_x$ samples. It is commonly known that the oxygen vacancy defects will be formed with the appearance of Ce^{3+} to maintain electrostatic balance according to Equation (1):

$$4Ce^{4+} + O^{2-} \rightarrow 4Ce^{4+} + 2e^- / \square + 0.5O_2 \rightarrow 2Ce^{4+} + 2Ce^{3+} + \square + 0.5O_2 \quad (1)$$

$\square$ represents the empty position by the removal of O^{2-} from the lattice (i.e., oxygen vacancy defect). It suggests that the oxygen vacancy defects formed for the $Ni_yCe_{100-y}O_x$ samples, which is consistent with the Raman results.

To test the electrochemical performance of $Ni_yCe_{100-y}O_x$ catalysts, the polarization curves of these catalysts (Figure 4a) were obtained using Linear Sweep Voltammetry (LSV). The overpotentials of the catalysts for the current density of 10 mA/cm^2 are listed in Table 1. The $Ni_{10}Ce_{90}O_x$ catalyst showed the lowest current density for the applied potentials and had the largest overpotential of 363 mV for the current density of 10 mA/cm^2. The overpotentials for the $Ni_{75}Ce_{25}O_x$ and $Ni_{50}Ce_{50}O_x$ catalysts were 338 mV and 341 mV to obtain the current density of 10 mA/cm^2, which were lower than that of other samples. The Tafel slope results of $Ni_yCe_{100-y}O_x$ catalysts were shown in Figure 4b and Table 1. The Tafel slopes of the $Ni_{75}Ce_{25}O_x$ and $Ni_{50}Ce_{50}O_x$ catalysts (66 mV/decade) were close to that of $Ni_{95}Ce_5O_x$, $Ni_{90}Ce_{10}O_x$ and $Ni_{25}Ce_{75}O_x$ catalysts (68 mV/decade), and were lower than that of the $Ni_{10}Ce_{90}O_x$ catalyst (73 mV/decade). An electrocatalyst with a low Tafel slope will have a small kinetic barrier for electron and mass transfer [2,5]. This indicates that the transfer barriers of electron and mass in the $Ni_{75}Ce_{25}O_x$ and $Ni_{50}Ce_{50}O_x$ catalysts are slightly improved.

The double-layer capacitance can be used to estimate the electrochemically active surface area (ECSA) of each sample. In order to know the double-layer capacitance, we first obtained CV curves of the capacitance current in the non-Faradaic voltage region (a 0.1 V potential range centered on the OCP) for several different scan rates (Figure 5). The rate of change in the current at OCP with respect to the scan rate corresponds to the double-layer capacitance [18]. For this reason, the current at OCP was plotted against the scan rate for the $Ni_yCe_{100-y}O_x$ catalysts, and a line of best fit was fitted for each catalyst's data set, as shown in Figure 4c. The double layer capacitance was 12.3 mF, 14.5 mF, 20.6 mF, 19.5 mF, 10.7 mF, and 7.1 mF for the $Ni_{95}Ce_5O_x$, $Ni_{90}Ce_{10}O_x$, $Ni_{75}Ce_{25}O_x$, $Ni_{50}Ce_{50}O_x$,

$Ni_{25}Ce_{75}O_x$, and $Ni_{10}Ce_{90}O_x$ samples, respectively. The ECSA can be calculated according to the formula ECSA = C_{DL}/C_s, where a specific capacitance of C_s = 0.040 mF cm^{-2} was used in this work [18]. The calculated ECSA values for the $Ni_yCe_{100-y}O_x$ catalysts as well as other relevant electrochemistry parameters are summarized in Table 1. The ECSAs of the $Ni_{75}Ce_{25}O_x$ and $Ni_{50}Ce_{50}O_x$ catalysts are similar and larger than that of other $Ni_yCe_{100-y}O_x$ catalysts. This is consistent with the observed current densities, as a larger ECSA means a sample has more active sites and therefore can catalyze more reactions at once and sustain a large current.

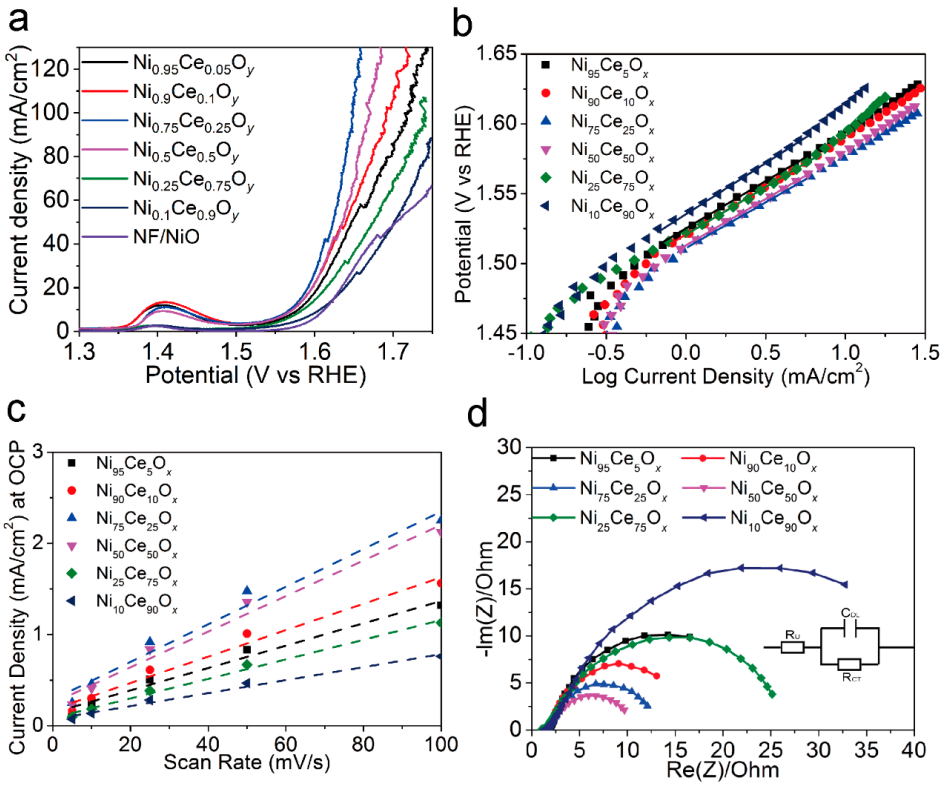

Figure 4. (**a**) Polarization curves of the NF/NiO substrate and $Ni_yCe_{100-y}O_x$ catalysts for the OER with a scan rate of 10 mV/s. (**b**) Tafel plots obtained from the steady–state polarization curves with a scan rate of 1 mV/s. (**c**) Current density at OCP vs. CV scan rate for $Ni_yCe_{100-y}O_x$ samples. The slope of current density at OCP vs. scan rate stands for the double–layer capacitance. (**d**) Nyquist plots of $Ni_yCe_{100-y}O_x$ samples obtained at 1.55 V vs. RHE. The inset is the electrical equivalent circuit.

Table 1. Electrochemically active surface area (ECSA), Tafel slope, mass-transfer resistance (R_{CT}) and the overpotential (η) for the current density of 10 mA/cm^2 for each catalyst investigated in 1 M KOH.

Catalyst	ECSA/cm^2	Tafel Slope	R_{CT}	η for 10 mA/cm^2
$Ni_{95}Ce_5O_x$	307.5 cm^2	68 mV/decade	18.2 Ω	351 mV
$Ni_{90}Ce_{10}O_x$	362.5 cm^2	68 mV/decade	12.6 Ω	350 mV
$Ni_{75}Ce_{25}O_x$	515 cm^2	66 mV/decade	9.9 Ω	338 mV
$Ni_{50}Ce_{50}O_x$	487.5 cm^2	66 mV/decade	7.5 Ω	341 mV
$Ni_{25}Ce_{75}O_x$	267.5 cm^2	68 mV/decade	21 Ω	356 mV
$Ni_{10}Ce_{90}O_x$	177.5 cm^2	73 mV/decade	31.8 Ω	363 mV

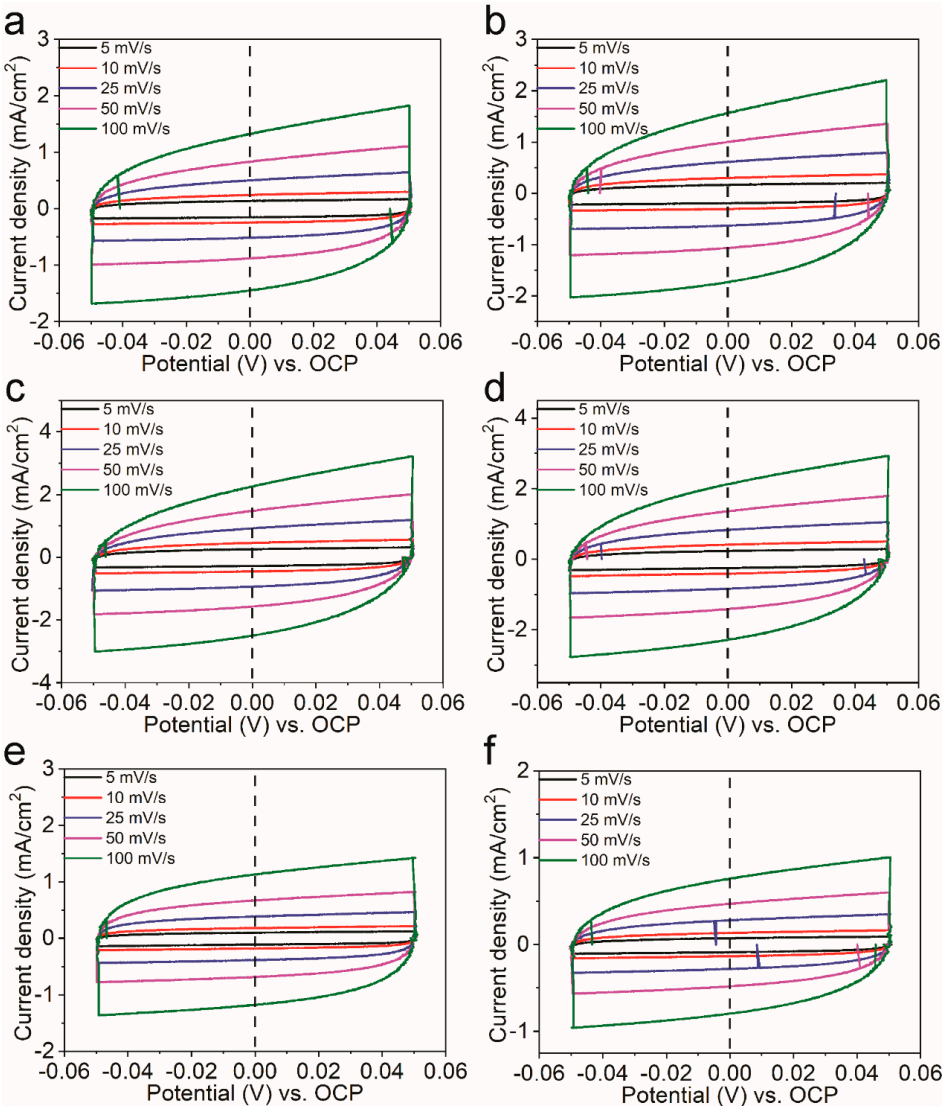

Figure 5. Cyclic voltammograms of (**a**) $Ni_{95}Ce_5O_x$, (**b**) $Ni_{90}Ce_{10}O_x$, (**c**) $Ni_{75}Ce_{25}O_x$, (**d**) $Ni_{50}Ce_{50}O_x$, (**e**) $Ni_{25}Ce_{75}O_x$ and (**f**) $Ni_{10}Ce_{90}O_x$ catalysts tested in a region with non–Faradaic process of the voltammogram with the scan rate of 5 mV/s, 10 mV/s, 25 mV/s, 50 mV/s and 100 mV/s. The value of the open circuit potential was 1.27 V vs. RHE.

The charge transfer resistance (R_{CT}) of the $Ni_yCe_{100-y}O_x$ catalysts were obtained from their Nyquist plots, as shown in Figure 4d. As shown in Table 1, the R_{CT} of the $Ni_yCe_{100-y}O_x$ catalysts decreased firstly and then increased with the increasing Ce content in the catalysts, and the $Ni_{50}Ce_{50}O_x$ catalyst had the lowest R_{CT} of 7.5 Ω at an applied bias of 1.55 V vs. RHE. The $Ni_{75}Ce_{25}O_x$ catalyst also showed a low R_{CT} of 9.9 Ω. However, the R_{CT} of the $Ni_{10}Ce_{90}O_x$ (31.8 Ω) catalyst was much higher than other $Ni_yCe_{100-y}O_x$ catalysts. The small mass-transfer resistance of the $Ni_{75}Ce_{25}O_x$ and $Ni_{50}Ce_{50}O_x$ catalysts stands for their favorable OER kinetics.

For the Ce-based catalysts, the oxygen mobility can be promoted by the generated oxygen vacancy defects, resulting an improved ionic conductivity [10]. Also, the oxygen vacancy defects can be act as the OER active sites to catalyze the water oxidation reaction [17]. Therefore, the larger concentration of oxygen vacancy defects results in the lower Tafel slopes, small mass-transfer resistance, and larger ECSAs of the $Ni_{75}Ce_{25}O_x$ and $Ni_{50}Ce_{50}O_x$ catalysts, which account for the higher OER activities for these two catalysts.

Controlled-current water electrolysis (Figure 6) was done to test the long-term performance and stability of the $Ni_{75}Ce_{25}O_x$ catalyst. With a fixed current density of 10 mA/cm^2,

the potential remained stable at 1.57 V vs. RHE for more than 100 h. This indicates that the $Ni_{75}Ce_{25}O_x$ catalyst is very stable during long-term water electrolysis.

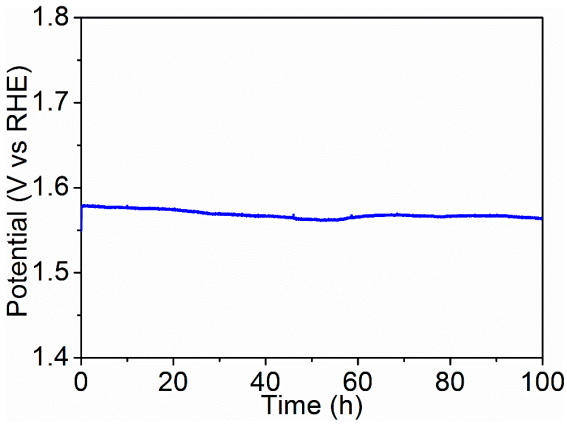

Figure 6. Potential trace of the $Ni_{75}Ce_{25}O_x$ sample obtained by fixing the current density for electrolysis at 10 mA/cm^2. The electrolyte was 1 M KOH (pH ≈ 14).

4. Conclusions

In summary, a series of NF/NiO/$Ni_yCe_{100-y}O_x$ catalysts were synthesized through the simple dip-coating and annealing methods. The oxygen vacancy defects are formed successfully in all the $Ni_yCe_{100-y}O_x$ catalysts, and the concentration of oxygen vacancy defects for $Ni_{75}Ce_{25}O_x$ and $Ni_{50}Ce_{50}O_x$ catalysts are larger than other $Ni_yCe_{100-y}O_x$ catalysts. This results in the larger electrochemically active surface areas for $Ni_{75}Ce_{25}O_x$ and $Ni_{50}Ce_{50}O_x$ catalysts because of the abundant active sites offered by the defects. The rich oxygen vacancy defects also improve the ionic conductivity so that a lower Tafel slope of 66 mV/decade is obtained for $Ni_{75}Ce_{25}O_x$ and $Ni_{50}Ce_{50}O_x$ catalysts. The improved ionic conductivity also results in the small mass-transfer resistance of $Ni_{75}Ce_{25}O_x$ and $Ni_{50}Ce_{50}O_x$ catalysts, which is favorable for their OER kinetics. Therefore, the $Ni_{75}Ce_{25}O_x$ and $Ni_{50}Ce_{50}O_x$ catalyst exhibit higher OER activity than other $Ni_yCe_{100-y}O_x$ catalysts with the overpotential of 338 mV and 341 mV for the current density of 10 mA/cm^2. With a fixed current density of 10 mA/cm^2, the potential remains stable at 1.57 V for more than 100 h, indicating the long-term stability of the $Ni_{75}Ce_{25}O_x$ catalyst.

Supplementary Materials: The following are available online at https://www.mdpi.com/2079-4991/11/2/437/s1, Figure S1: SEM images of $Ni_{90}Ce_{10}O_x$, $Ni_{75}Ce_{25}O_x$, $Ni_{50}Ce_{50}O_x$, $Ni_{25}Ce_{75}O_x$ and $Ni_{10}Ce_{90}O_x$ catalysts, Table S1: Atomic ratios of Ce, Ni and O in $Ni_yCe_{100-y}O_x$ catalysts derived from XPS results, Table S2: Raman peak areas at 563 cm^{-1} of $Ni_yCe_{100-y}O_x$ catalysts.

Author Contributions: Conceptualization, J.Y. and Q.C.; methodology, J.Y.; validation, J.Y., C.Q. and L.C.; formal analysis, J.Y.; investigation, J.Y.; resources, J.Y.; data curation, J.Y. and C.Q.; writing—original draft preparation, J.Y.; writing—review and editing, J.Y. and Q.C.; supervision, J.-J.D. and L.C.; project administration, J.Y. and Q.C.; funding acquisition, J.Y., Q.C. and J.-J.D. All authors have read and agreed to the published version of the manuscript.

Funding: Part of this research was funded by the JSPS Core-to-Core program (Advanced Research Networks type A), Japan (JSPS)-Korea (NRF) Bilateral program and Grants-in-Aids for Specially Promoted Research and KAKENHI (Grant number: 17H03229). Part of this research was funded by China Postdoctoral Science Foundation (Grant number: 2019M660297), and Fundamental Research Funds for the Central Universities of Ministry of Education of China (Southeast University).

Acknowledgments: The XRD and electron microscopy characterizations were conducted at the Advanced Characterization Nanotechnology Platform of the University of Tokyo, supported by "Nanotechnology Platform" of the Ministry of Education, Culture, Sports, Science and Technology (MEXT), Japan.

Conflicts of Interest: The authors declare no conflict of interest.

References

1. Suen, N.T.; Hung, S.F.; Quan, Q.; Zhang, N.; Xu, Y.J.; Chen, H.M. Electrocatalysis for the oxygen evolution reaction: Recent development and future perspectives. *Chem. Soc. Rev.* **2017**, *46*, 337–365. [CrossRef] [PubMed]
2. Li, C.; Cao, Q.; Wang, F.; Xiao, Y.; Li, Y.; Delaunay, J.-J.; Zhu, H. Engineering graphene and TMDs based van der Waals heterostructures for photovoltaic and photoelectrochemical solar energy conversion. *Chem. Soc. Rev.* **2018**, *47*, 4981–5037. [CrossRef]
3. Yu, J.; Wang, J.; Long, X.; Chen, L.; Cao, Q.; Wang, J.; Qiu, C.; Lim, J.; Yang, S. Formation of FeOOH Nanosheets Induces Doping of CeO_{2-x} with High-Valence Ni for Efficient Water Oxidation. *Adv. Energy Mater.* **2021**, *11*, 2002731. [CrossRef]
4. Cao, Q.; Che, R.; Chen, N. Scalable synthesis of Cu_2S double-superlattice nanoparticle systems with enhanced UV/visible-light-driven photocatalytic activity. *Appl. Catal. B* **2015**, *162*, 187–195. [CrossRef]
5. Yu, J.; Cao, Q.; Feng, B.; Li, C.; Liu, J.; Clark, J.K.; Delaunay, J.-J. Insights into the efficiency and stability of Cu-based nanowires for electrocatalytic oxygen evolution. *Nano Res.* **2018**, *11*, 4323–4332. [CrossRef]
6. Hao, S.; Liu, J.; Cao, Q.; Zhao, Y.; Zhao, X.; Pei, K.; Zhang, J.; Chen, G.; Che, R. In-situ electrochemical pretreatment of hierarchical Ni_3S_2-based electrocatalyst towards promoted hydrogen evolution reaction with low overpotential. *J. Colloid Interface Sci.* **2020**, *559*, 282–290. [CrossRef] [PubMed]
7. Hao, S.; Cao, Q.; Yang, L.; Che, R. Morphology-optimized interconnected Ni_3S_2 nanosheets coupled with $Ni(OH)_2$ nanoparticles for enhanced hydrogen evolution reaction. *J. Alloys Compd.* **2020**, *827*, 154163. [CrossRef]
8. Yuan, K.; Cao, Q.; Lu, H.-L.; Zhong, M.; Zheng, X.; Chen, H.-Y.; Wang, T.; Delaunay, J.-J.; Luo, W.; Zhang, L.; et al. Oxygen-deficient WO_{3-x}@TiO_{2-x} core–shell nanosheets for efficient photoelectrochemical oxidation of neutral water solutions. *J. Mater. Chem. A* **2017**, *5*, 14697–14706. [CrossRef]
9. Qiu, B.; Wang, C.; Zhang, N.; Cai, L.; Xiong, Y.; Chai, Y. CeO_2-Induced Interfacial Co^{2+} Octahedral Sites and Oxygen Vacancies for Water Oxidation. *ACS Catal.* **2019**, *9*, 6484–6490. [CrossRef]
10. Yu, J.; Cao, Q.; Li, Y.; Long, X.; Yang, S.; Clark, J.K.; Nakabayashi, M.; Shibata, N.; Delaunay, J.-J. Defect-Rich $NiCeO_x$ Electrocatalyst with Ultrahigh Stability and Low Overpotential for Water Oxidation. *ACS Catal.* **2019**, *9*, 1605–1611. [CrossRef]
11. Yuan, K.; Zhu, L.-Y.; Cao, Q.; Ma, H.-P.; Tao, J.-J.; Huang, W.; Lu, H.-L. ALD-based hydrothermal facile synthesis of a dense WO_3@TiO_2–Fe_2O_3 nanodendrite array with enhanced photoelectrochemical properties. *J. Mater. Chem. C* **2020**, *8*, 6756–6762. [CrossRef]
12. Xu, L.; Jiang, Q.; Xiao, Z.; Li, X.; Huo, J.; Wang, S.; Dai, L. Plasma-Engraved Co_3O_4 Nanosheets with Oxygen Vacancies and High Surface Area for the Oxygen Evolution Reaction. *Angew. Chem. Int. Ed.* **2016**, *55*, 5277–5281. [CrossRef]
13. Yu, J.; Si, Z.; Chen, L.; Wu, X.; Weng, D. Selective catalytic reduction of NO_x by ammonia over phosphate-containing $Ce_{0.75}Zr_{0.25}O_2$ solids. *Appl. Catal. B* **2015**, *163*, 223–232. [CrossRef]
14. Yu, J.; Si, Z.; Li, X.; Chen, L.; Wu, X.; Weng, D. Effect of lean-oxygen treatment on the adsorption and activity of zirconium phosphate @ $Ce_{0.75}Z_{0.25}O_2$ for NH_3-SCR deNO_x. *Catal. Today* **2016**, *267*, 47–55. [CrossRef]
15. Yu, J.; Si, Z.; Zhu, M.; Wu, X.; Chen, L.; Weng, D.; Zou, J. NH_3-SCR activity, hydrothermal stability and poison resistance of a zirconium phosphate/$Ce_{0.5}Zr_{0.5}O_2$ catalyst in simulated diesel exhaust. *RSC Adv.* **2015**, *5*, 83594–83599. [CrossRef]
16. Yuan, K.; Wang, C.-Y.; Zhu, L.-Y.; Cao, Q.; Yang, J.-H.; Li, X.-X.; Huang, W.; Wang, Y.-Y.; Lu, H.-L.; Zhang, D.W. Fabrication of a Micro-Electromechanical System-Based Acetone Gas Sensor Using CeO_2 Nanodot-Decorated WO_3 Nanowires. *ACS Appl. Mater. Interfaces* **2020**, *12*, 14095–14104. [CrossRef] [PubMed]
17. Yu, J.; Wang, Z.; Wang, J.; Zhong, W.; Ju, M.; Cai, R.; Qiu, C.; Long, X.; Yang, S. The Role of Ceria in a Hybrid Catalyst toward Alkaline Water Oxidation. *ChemSusChem* **2020**, *13*, 5273–5279. [CrossRef]
18. McCrory, C.C.; Jung, S.; Peters, J.C.; Jaramillo, T.F. Benchmarking Heterogeneous Electrocatalysts for the Oxygen Evolution Reaction. *J. Am. Chem. Soc.* **2013**, *135*, 16977–16987. [CrossRef]
19. Li, Q.; Huang, Z.; Guan, P.; Su, R.; Cao, Q.; Chao, Y.; Shen, W.; Guo, J.; Xu, H.; Che, R. Simultaneous Ni Doping at Atom Scale in Ceria and Assembling into Well-Defined Lotuslike Structure for Enhanced Catalytic Performance. *ACS Appl. Mater. Interfaces* **2017**, *9*, 16243–16251. [CrossRef] [PubMed]
20. Guo, M.; Lu, J.; Wu, Y.; Wang, Y.; Luo, M. UV and Visible Raman Studies of Oxygen Vacancies in Rare-Earth-Doped Ceria. *Langmuir* **2011**, *27*, 3872–3877. [CrossRef] [PubMed]
21. Nakajima, A.; Yoshihara, A.; Ishigame, M. Defect-induced Raman spectra in doped CeO_2. *Phys. Rev. B* **1994**, *50*, 13297–13307. [CrossRef] [PubMed]
22. Spanier, J.E.; Robinson, R.D.; Zhang, F.; Chan, S.-W.; Herman, I.P. Size-dependent properties of CeO_{2-y} nanoparticles as studied by Raman scattering. *Phys. Rev. B* **2001**, *64*, 245407. [CrossRef]
23. He, L.; Liang, B.; Li, L.; Yang, X.; Huang, Y.; Wang, A.; Wang, X.; Zhang, T. Cerium-Oxide-Modified Nickel as a Non-Noble Metal Catalyst for Selective Decomposition of Hydrous Hydrazine to Hydrogen. *ACS Catal.* **2015**, *5*, 1623–1628. [CrossRef]
24. Filtschew, A.; Hofmann, K.; Hess, C. Ceria and Its Defect Structure: New Insights from a Combined Spectroscopic Approach. *J. Phys. Chem. C* **2016**, *120*, 6694–6703. [CrossRef]
25. Liu, X.; Zhou, K.; Wang, L.; Wang, B.; Li, Y. Oxygen Vacancy Clusters Promoting Reducibility and Activity of Ceria Nanorods. *J. Am. Chem. Soc.* **2009**, *131*, 3140–3141. [CrossRef]